Eik, Marika; Antonova, Anna; Puttonen, Jari

Phase contrast tomography to study near-field effects of polypropylene fibres on hardened cement paste

Published in:
Cement and Concrete Composites

DOI:
10.1016/j.cemconcomp.2020.103800

Published: 01/11/2020

Document Version
Publisher's PDF, also known as Version of record

Cement and Concrete Composites 114 (2020) 103800

Contents lists available at ScienceDirect

Cement and Concrete Composites

journal homepage: http://www.elsevier.com/locate/cemconcomp

Phase contrast tomography to study near-field effects of polypropylene fibres on hardened cement paste

Marika Eik *, Anna Antonova, Jari Puttonen **

Civil Engineering Department, Aalto University School of Engineering, Rakentajanaukio 4 A, Otaniemi, 02150, Espoo, Finland

ARTICLE INFO

Keywords:
phase Contrast imaging
Tomography
Cement paste
Fibre
Interfacial transition zone
Image analysis

ABSTRACT

In this study the boundary zone around polypropylene fibres in hardened cement paste was defined in terms of porosity and unhydrated cement particles using the phase contrast tomography with a spatial resolution of 0.637 μm within a volume of $1.305 \times 1.305 \times 1.305$ mm^3. Pores and unhydrated grains were identified from the cement paste made of blended cement by separating them from computed tomography images using thresholding method. In the identification of the gray-level ranges of pores and unhydrated particles several approaches, such as tangent-slope and overflow criterion including the cumulative curve of the gray-level image, were utilised. The changes in relative amounts of pores and unhydrated particles indicated that the boundary zone extended to a distance of 70 μm from the fibre surface. Within the boundary zone, the porosity was about twice or even four times higher than in the bulk cement paste. The volume fraction of pores was observed to vary from 7% to 35% close to the fibre, where the pores were also typically interconnected with the resolution used. Compared to bulk cement paste, the amount of pores exceeding a volume of 10^5 μm^3 increased in the boundary zone. Close to the fibre surface, the volume fraction of unhydrated particles was about 2% being 33% of the value outside the boundary zone.

1. Introduction

The use of X-ray computed tomography (CT) allows to study non-transparent materials three-dimensionally without destroying their internal micro-structure. The artefacts from cutting, grinding, and polishing of samples, which may occur with scanning electron microscopy, can be avoided by CT. The accuracy of CT images depends on technical configurations of a tomograph, the reconstruction algorithm applied on projection images, and on the size and density of the sample scanned. For example, with a larger and denser sample the attenuation of X-ray increases and less photons are reaching the detector, which significantly reduces image quality [41]. The contrast and spatial resolution of CT images are improved if an X-ray beam is monochromatic and focused. The coherent radiation provided by the synchrotron facility makes it possible to use phase contrast tomography for imaging. The principle difference of phase contrast tomography from a conventional transmission X-ray imaging is the use of X-ray wave to detect the phase shift, i.e. change in the propagation direction of a wave-front [23]. The phase shift is proportional to material density and occurs at the edges of particles or pores, where material has different index of refraction. The magnitude of the X-ray phase shift is sufficiently large even if the absorption cannot be detected [23]. The sensitivity of phase contrast tomography allows to study the materials consisting of various components with small differences in their densities.

The effect of a fibre on a cementitious matrix depends on the interaction between them [3,13]. This interaction affects the formation of the micro-structure and mineralogical composition of the cement paste around the fibre surface by creating a boundary zone, called the interfacial transition zone (ITZ) [2,43]. The ITZ also surrounds other inclusions in cementitious matrix, such as aggregates. X-ray CT has been used to study the micro-structure of the cement paste in three-dimensions, as reported by Ref. [5,12,20,32,44]. In Ref. [20] X-ray synchrotron tomography was used to study the packing of the cement particles close to the inclusion surface. Cement was cast into the glass tube with an inner diameter of 0.5 mm and scanned in 5 min by X-ray synchrotron. The field of scanning was 0.8×0.6 mm^2, and the resolution received was 0.33 μm. The authors assumed that the ITZ was lack of large particles from the very beginning of hydration, as the

* Corresponding author.
** Corresponding author.
E-mail addresses: marika.eik@aalto.fi (M. Eik), anna.antonova@aalto.fi (A. Antonova), jari.puttonen@aalto.fi (J. Puttonen).

https://doi.org/10.1016/j.cemconcomp.2020.103800
Received 18 December 2019; Received in revised form 18 June 2020; Accepted 24 August 2020
Available online 3 September 2020

Table 1
Chemical composition of the cement used.

Oxides (%)	CaO	SiO_2	Al_2O_3	Fe_2O_3	MgO	SO_3	TiO_2	Na_2O	K_2O
Clinker[a]	64	21	5.2	3.3	3.2	3.3	–	–	–
Slag[a]	39	38	9	–	11	1	1	0.5	0.5
Limestone[b]	90	5	1.5	–	2.5	–	–	1	–

[a] According the information provided by the manufacturer [9,10].
[b] Determined with the EDX point analysis.

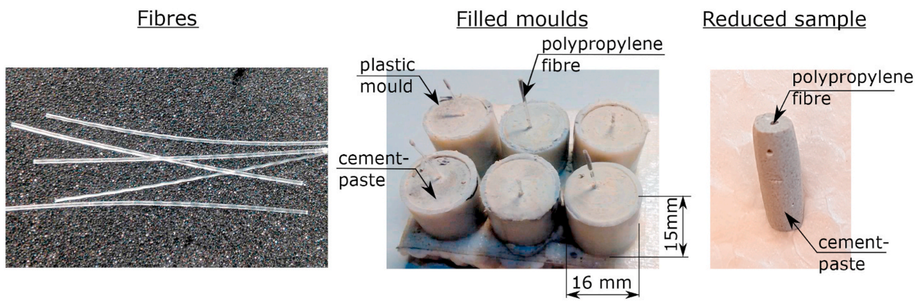

Fig. 1. Polypropylene fibres used, preparation of the samples for CT scanning.

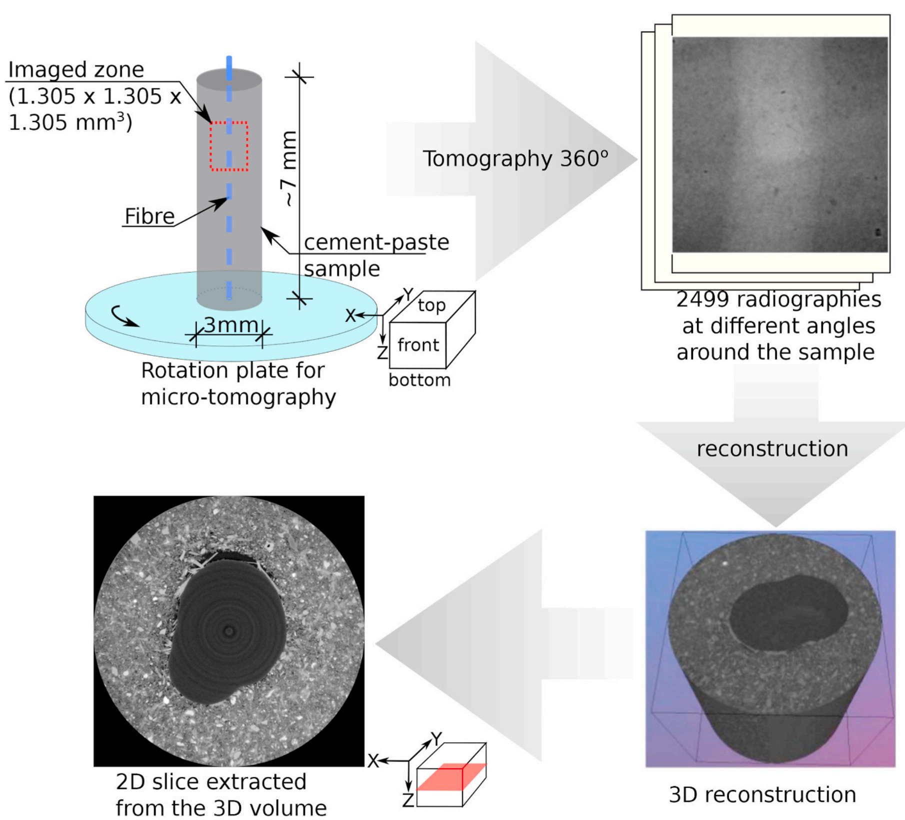

Fig. 2. The placement of the sample during the scanning and the reconstruction of the whole volume considering the phase estimation.

hydrodynamic forces repelled the particles from the inclusion surface. In the study, large cement particles were not observed closer than 20 μm from the glass wall. In Ref. [15,16], plain and fibre reinforced samples of cement mortar were examined by synchrotron tomography to study the progress and effect of alkali-silica reaction during the period of 2–136 days after cast. In the study, polypropylene fibres represented hydrophobic fibres whereas hydrophilic fibres were polypropylene fibres coated by ethylene acrylic acid. The pixel size 3.32 μm was received on the 8.3 mm field of view. The tomographic slices and 3D reconstructed and segmented images demonstrated the distribution of air voids, the formation and propagation of cracks, the progress of aggregate dissolution and silica gel formation. The study found that the content of air bubbles in fibre reinforced mortars was higher than that in the plain mortar, which reduced expansion due to the voids into which the alkali-silica gel could migrate. The hybrid fibres had a bundled distribution whereas the distribution of polypropylene fibres was more uniform. The agglomerated behaviour of hybrid fibres was assumed to be related to their aspect ratio and the hydrophilic properties.

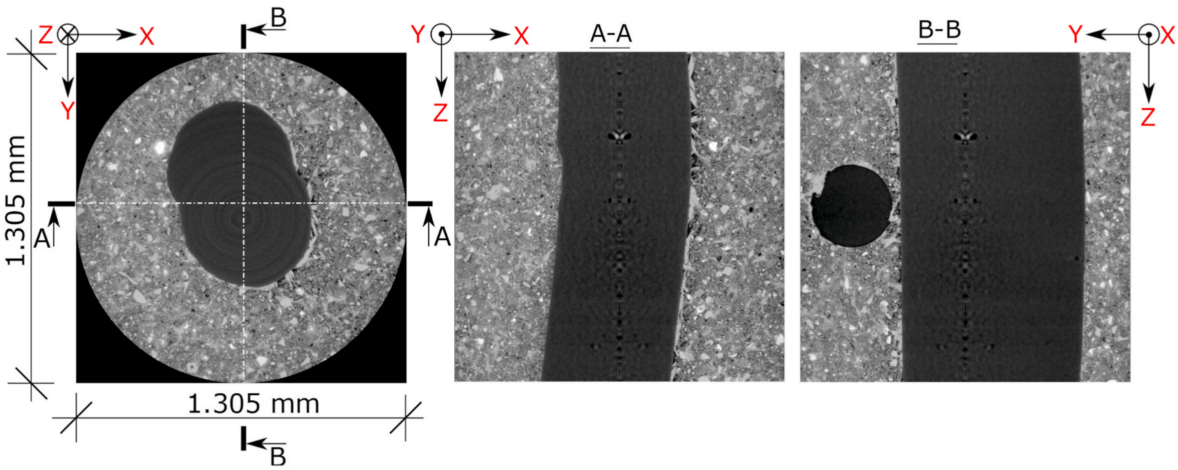

(a) Sample S1.

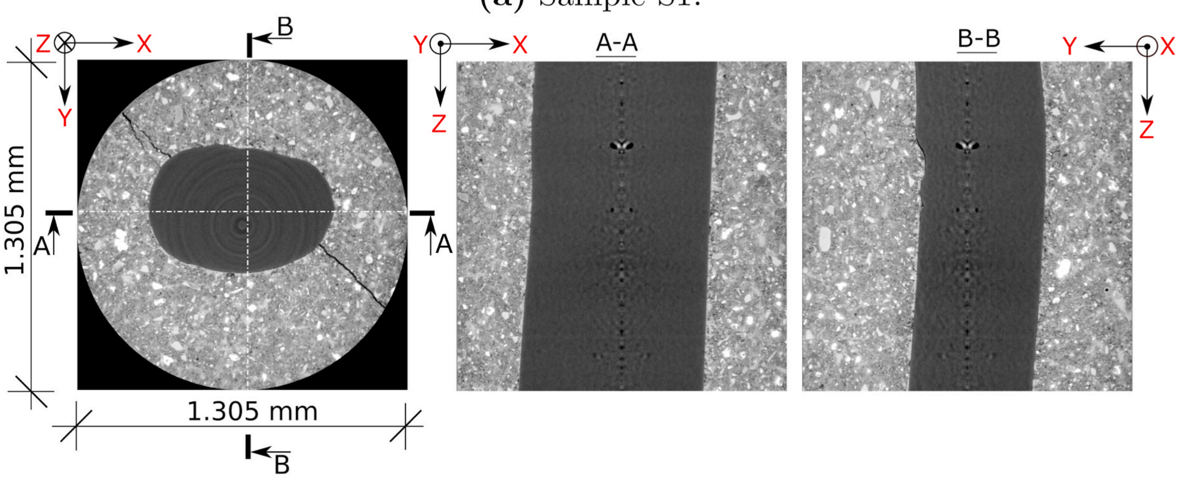

(b) Sample S2.

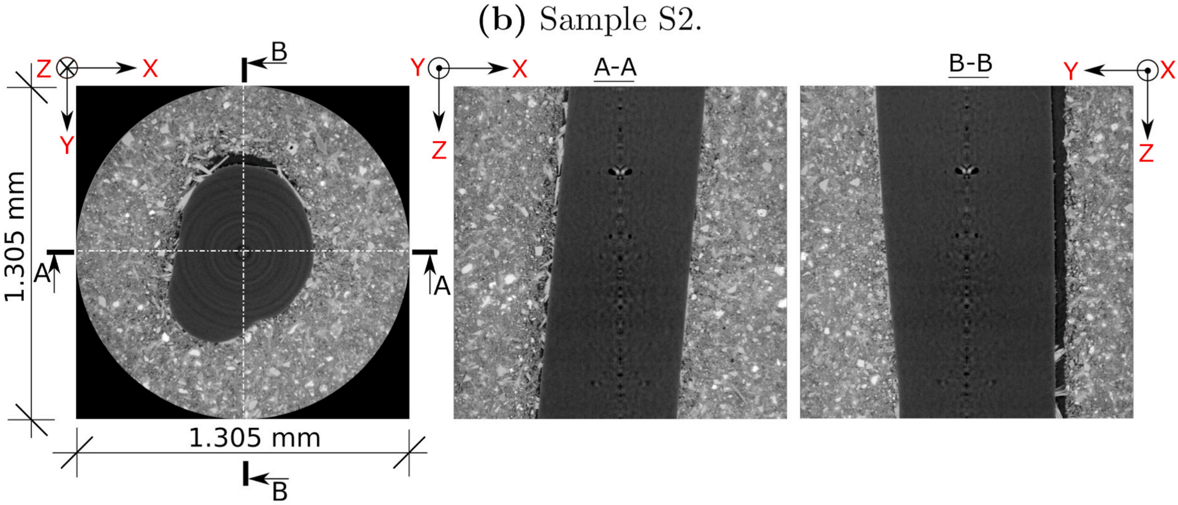

(c) Sample S3.

Fig. 3. The slices with the orthogonal sections of the samples with polypropylene fibres.

As the ITZ around the different fibre types or aggregates was not been emphasised in CT applications to cementitious composites, the previous studies have reported the findings obtained from pure cement paste or mortar considering neither the interface nor the boundary effect. The motivation for this work was to define the boundary zone created by polypropylene fibres in the hardened cement paste by applying the phase contrast synchrotron tomography. Even if this type of imaging technique has been seldom used for the cement paste, it is a robust and suitable method for studying the micro-structure of cementitious composites. In this study, the boundary zone around the fibre was recognised

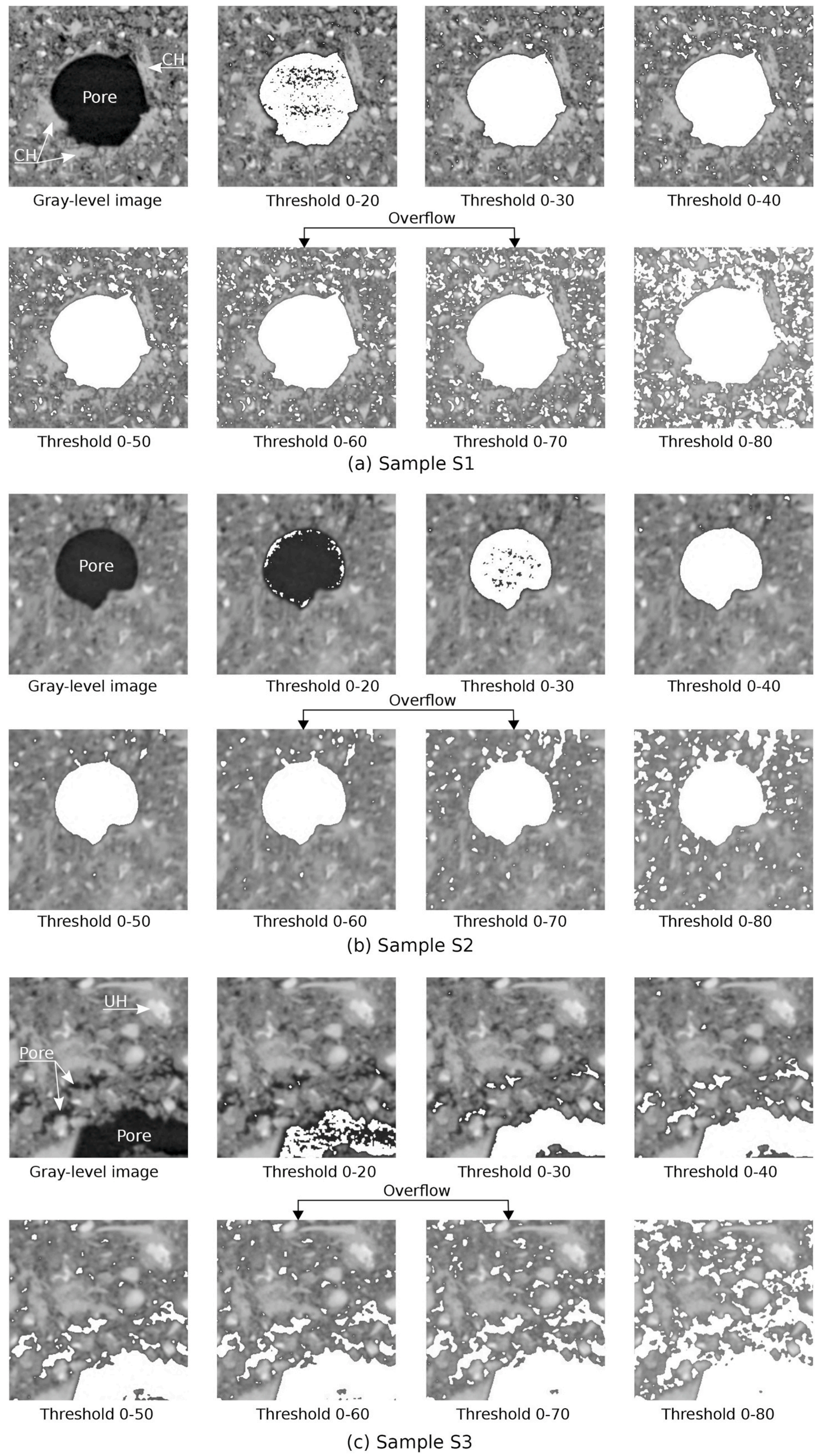

Fig. 4. The overflow criterion of pores thresholded with different upper thresholds.

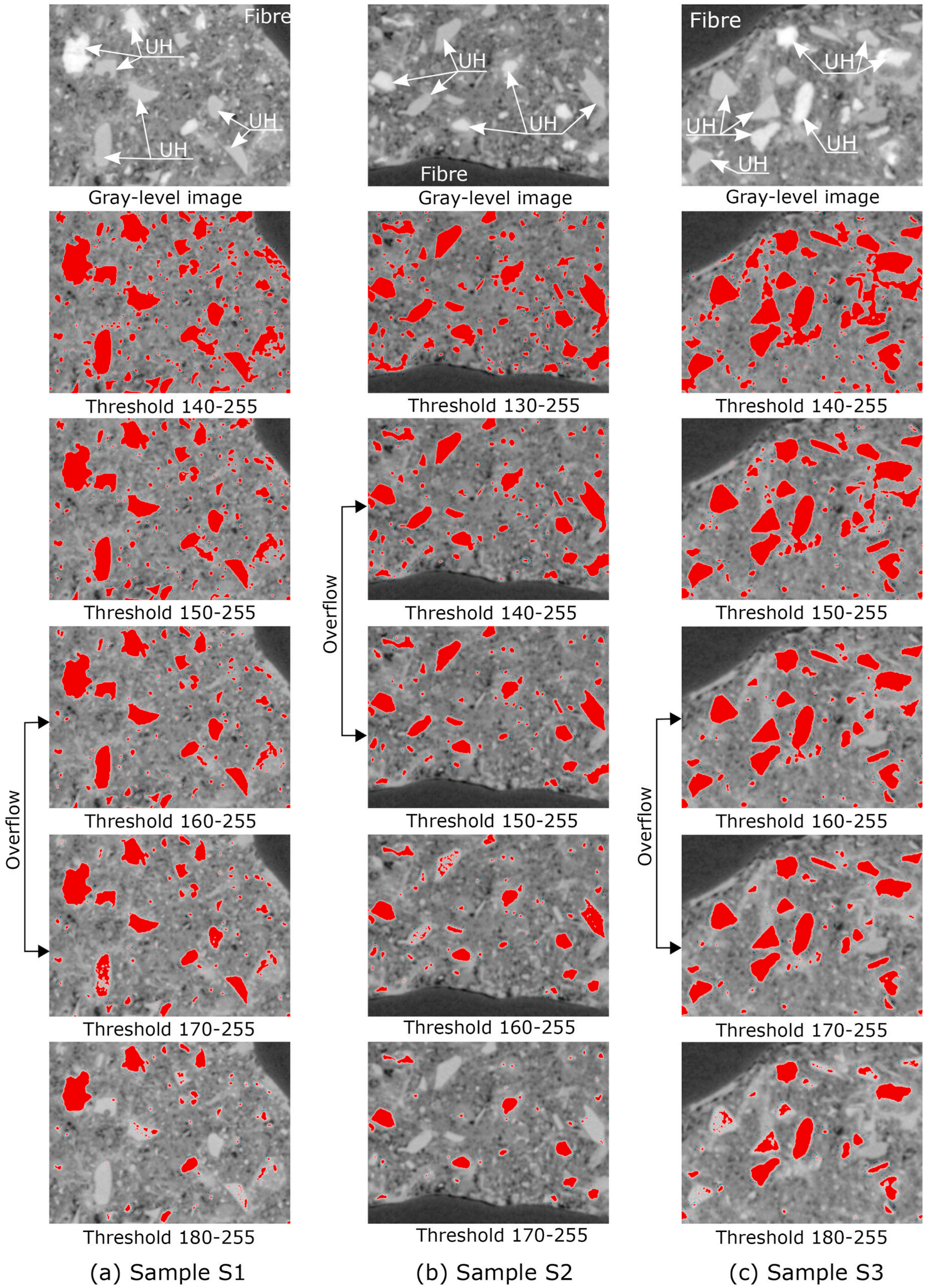

Fig. 5. The overflow criterion of UH particles thresholded with different lower thresholds.

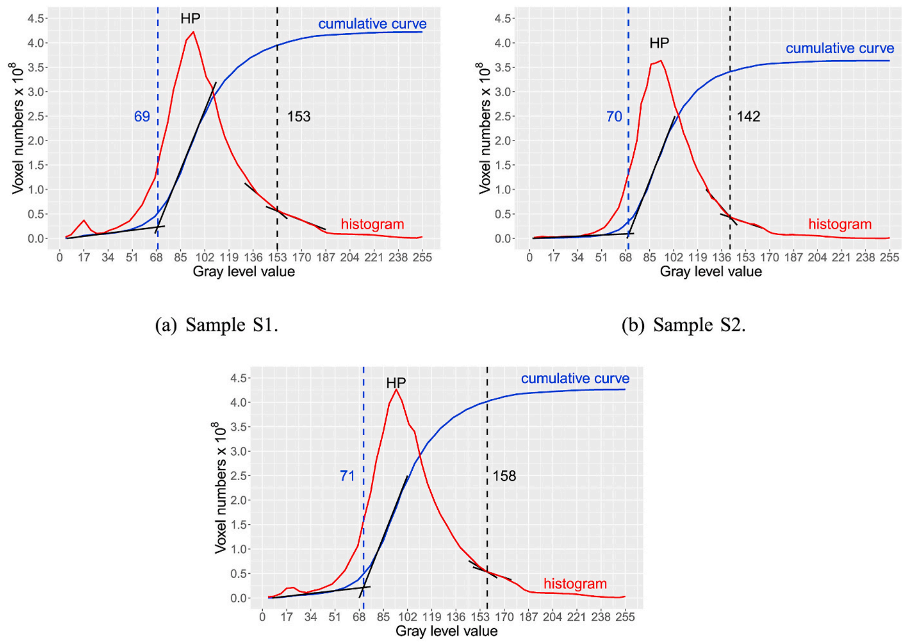

(a) Sample S1.

(b) Sample S2.

(c) Sample S3.

Fig. 6. The cumulative curves to separate the pores and the gray-level histograms to separate the HP and UH particles.

by defining the gradients of porosity and unhydrated (UH) cement particles from the three-dimensional data measured close to the fibre surface. The slag cement used with limestone is a typical mixture for concretes of higher strength and for massive structural members, since it can reduce the size of largest pores and affect the porosity, as well as decrease the hydration temperature [2]. The relative distributions of pores and UH particles describe the influence of the fibre surface both on the packing of the cement grains and hydration close to the fibre, and can be utilised for developing the cement blends for fibre reinforced cementitious composites. The information of the relative distribution of pores within the transition zone is also relevant for evaluating the durability, shrinkage and strength of the final composite. Polypropylene fibres used in the samples are often utilised in structural applications, where the visible fibre corrosion should be avoided, such as elements of building facades. They have also been used for limiting the spalling of high strength concrete at elevated temperatures and for reinforcing the thin-walled structures, and the structures with complex geometrical shapes [8,14,18,24].

Essentially, it is difficult to obtain tomography images with a resolution smaller than 1 μm from the cementitious composite samples with reasonable dimensions, especially utilising CT devices typically available in research laboratories [19]. For example, in Ref. [40,45] the resolutions of CT images obtained by scanning of the cement paste samples with a thicknesses of 0.25 mm and 10 mm were 0.485 μm and 15.2 μm, respectively. In the studies documented in Ref. [12,20,28] the resolutions of the scans obtained by synchrotron radiation facility from the cement paste samples with a thickness of 0.5 and 0.6 mm were 0.33 μm and 0.6835 μm, respectively, and in case of crashed samples it was 0.5 μm. In this study we utilised high resolution three-dimensional images of the cement paste volumes equal to $1.305 \times 1.305 \times 1.305$ mm^3 from the samples with a diameter of 3 mm and a height of 7 mm. The resolution of CT images obtained was 0.637 μm, which allowed to analyse large capillaries and interfacial pores around the polypropylene fibres. The cement blend with slag and limestone was expected to affect the transition zone through the formation of calcium carbo-aluminate hydrates, which could reduce the porosity [2]. It was found that in cements blended with slag or fly ash, the locally increased water to cement (w/c) ratio close to the inclusion surface supported the formation of calcium aluminate hydrate (CAH) rather than the ettringite. This is a positive feature when the calcareous admixtures, for example, limestone powder (calcium carbonate), are added [2], as they need CAH to start to react. The results of their reaction are calcium carboaluminate hydrates. These can reduce porous spaces in the transition zone, as the reactions of calcium carbonate bind water increasing the total volume of solid phase [2,17]. Based on the X-ray diffraction and SEM, authors in Ref. [22] concluded that with the ordinary Portland (OP) cement, a high porosity within the ITZ resulted from the localised bleeding. The effect of mineral admixtures, such as granulated blast furnace slag, fly ash and condensed silica fume (SF), on the ITZ around the aggregate was also examined. The use of blended cements was found to reduce a relative thickness of the ITZ, but the reduction depended on the type and dosage of mineral admixture, and the age of curing.

2. Materials and methods

2.1. Cement-paste samples with polypropylene fibres

Cement, water and polypropylene fibres were used to prepare the samples. Plus-sementti [10] or CEM II/B-M (S-LL) 42,5 N (according to standard SFS-EN 197-1: 2011) was used in mixes. The chemical composition of the cement clinker and the content of other main constituents are represented in Table 1. The cement paste had a w/c ratio of 0.50. The polypropylene fibres used had an elliptical section with a width of 0.8 mm, height of 0.4 mm and the area of 0.251 mm^2 (Fig. 1).

The samples were moulded into cylindrical plastic forms with a diameter of 16 mm and a height of 15 mm. The forms and the fibres were fixed to polystyrene plate (Fig. 1). Each fibre was placed at the centre of the form. After casting, the samples were vibrated on the vibration table and covered with a plastic film. At the age of 24 h, the samples were placed into the environmental room with relative humidity of 95% and temperature $+ 20^{\circ}C$, and after 28 days of curing they were de-moulded.

To achieve the desired resolution of CT images, the diameter of the sample could be up to 3 mm, which was the reason for using the cement paste as a sample material instead of concrete. The bottom and the edges of the samples were cut by a low-speed diamond saw to decrease their

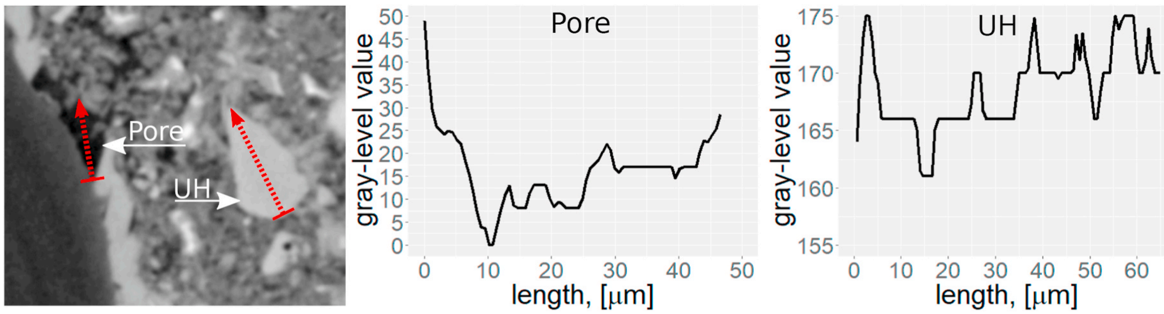

(a) Sample S1. Measured thresholds: pores 0-49, UH particles 161-175.

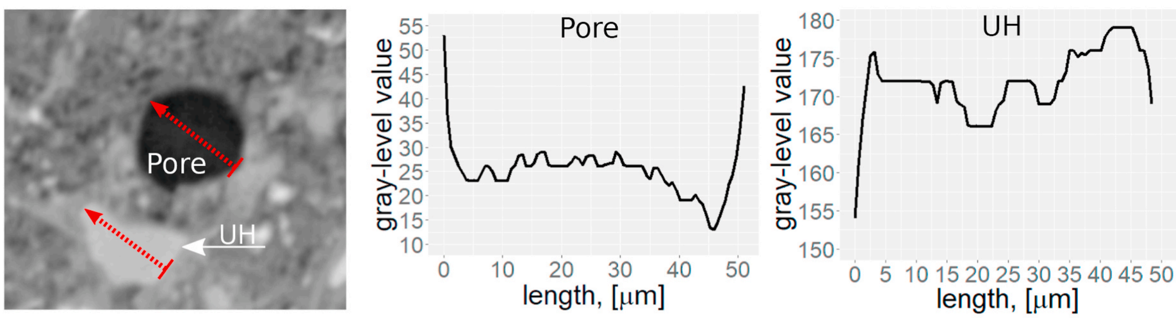

(b) Sample S2. Measured thresholds: pores 0-53, UH particles 154-179.

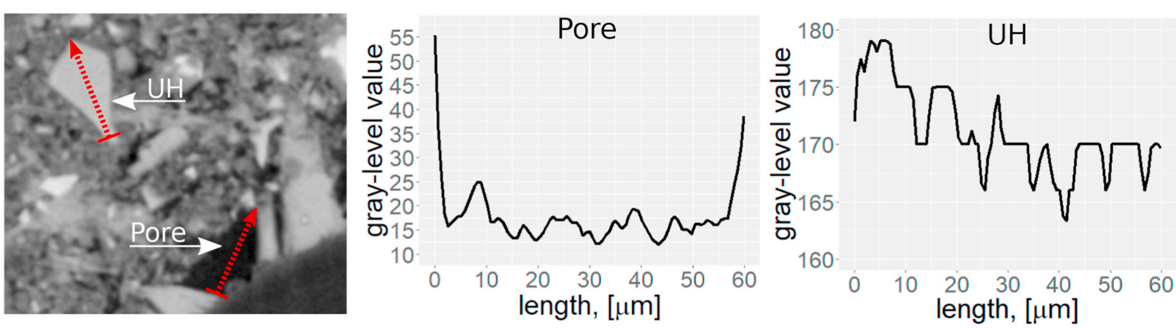

(c) Sample S3. Measured thresholds: pores 0-55, UH particles 163-179.

Fig. 7. Measuring the gray-level thresholds of pores and UH particles along the lines crossing the individual particles.

diameter and length. Sand-papers with grit sizes of P80 (201 μm), P240 (58.5 $\pm$ 2 μm) and P400 (35.0 $\pm$ 1.5 μm) were used to reduce the diameter of each sample up to about 3 mm in diameter (Fig. 1). Altogether, three samples with polypropylene fibres named as S1, S2, S3 were prepared.

2.2. Computed tomography to study the micro-structure of the cement paste

The synchrotron radiation facility emits highly coherent, monochromatic and parallel radiation [12,19]. A high degree of coherence, which provides a very small source size, allows to combine absorption tomography with phase contrast imaging. The use of synchrotron light enables to reduce the acquisition time and obtain the absorption images with improved spatial resolution resulting from the effective pixel size of detector.

To enhance the contrast between various material components along their boundaries in the absorption image, the phase images can be recorded in edge detection regime. A more sophisticated way to determine unambiguously the local phase shift of the wave-front is the phase retrieval approach, which separates the phase and the attenuation contrast of a material component. To obtain a phase retrieval image it is necessary to adapt the distance between the sample and the detector, and also to use a specific algorithm to reconstruct the volumes [27].

In the present study, the scanning of the samples was made at the European Synchrotron Radiation Facility (ESRF) using the beam line ID19. The scans were performed with the energy of 35 keV. The scintillator used was a Gadolinium Gallium Garnet Eu-doped (Gd3Ga5O12:Eu) with a thickness of 10 μm, which converted the X-rays to visible light. The camera was sCMOS (PCO.edge) with a physical pixel size of 6.5 μm and a detector size of 2560 $\times$ 2160 px^2. The images were recorded using the phase retrieval regime with the sample-to-detector distance equal to 50 mm. Standard optics of the microscopy were used with a total magnification of 10. 2499 projection images were obtained within the imaged zone of 1.305 $\times$ 1.305 $\times$ 1.305 mm^3 with the angle-step of 0.144° (Fig. 2). The exposure time was 0.03 s. The reconstruction of the whole volume considering the phase estimation technique was made by the algorithm developed at the ESRF [27]. To correct

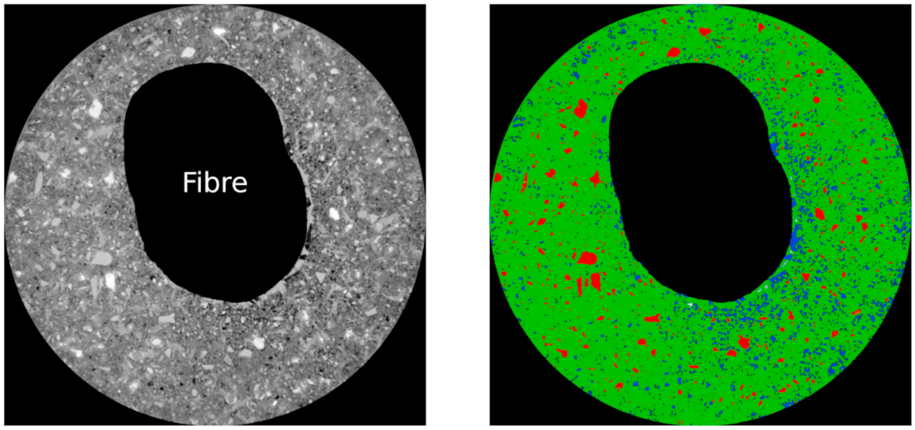

(a) Sample S1.

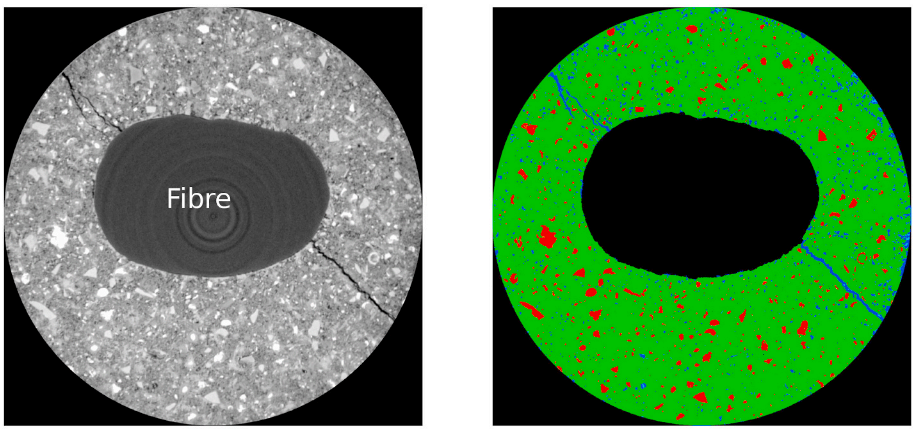

(b) Sample S2.

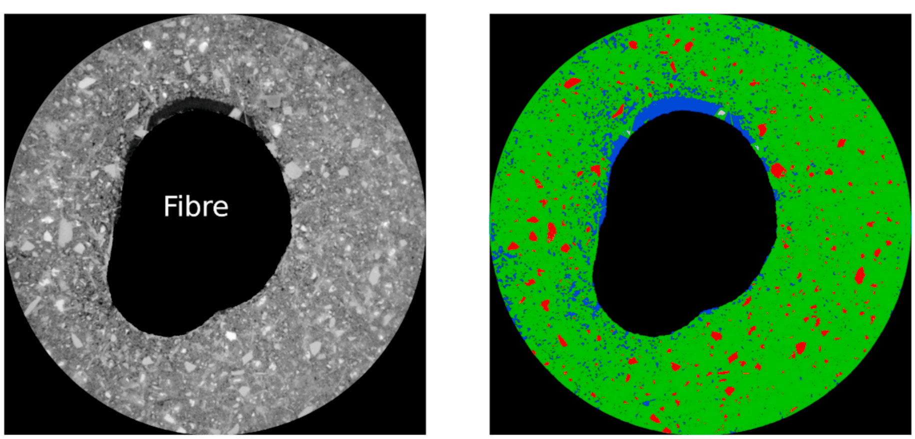

(c) Sample S3.

Fig. 8. The slices with thresholded pores (blue) and UH particles (red) based on the final gray-levels. Pores: 62, 63, 64, UH particles: 161, 147, 163 in the samples S1, S2 and S3, respectively. HP are marked by green colour. (For interpretation of the references to colour in this figure legend, the reader is referred to the Web version of this article.)

images and remove the artefacts appearing during the reconstruction of a volume, a specific software applying the algorithms based on the classical methods was used [25]. The slices with the orthogonal sections of the scanned samples are represented in Fig. 3.

2.3. Processing and analysis of CT images

In CT images, the separation to different material components can be done based on the intensity of brightness or darkness of each pixel, which depends on a mass density of the component. The denser is a material component, the brighter is the pixel representing it and vice versa. The intensity of brightness or darkness of each pixel can be defined by the gray-level value ranging from 0 to 255. In 8-bit grayscale system 0 corresponds to black colour and 255 corresponds to white, and for all the other gradations of intensities numeric values lie between these numbers.

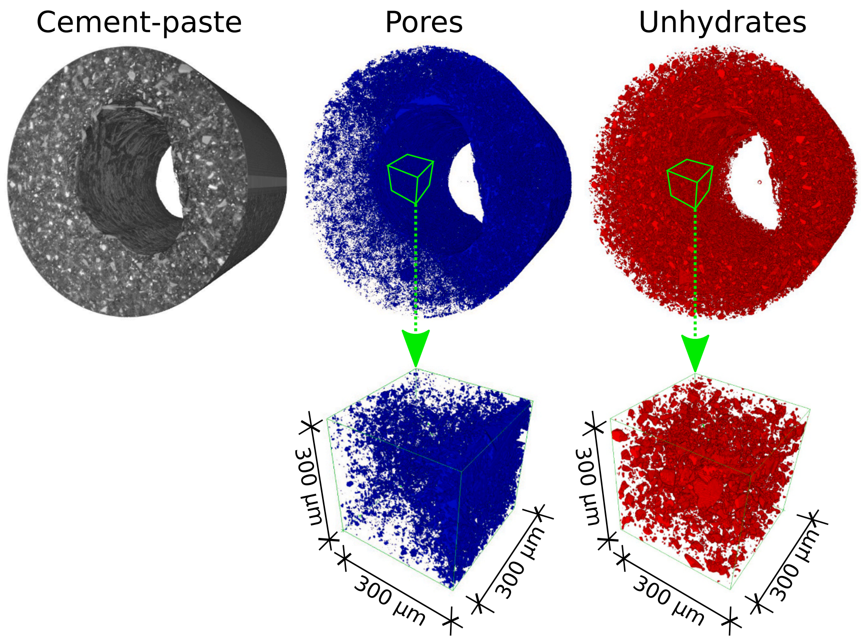

Fig. 9. Sample S3. The segmented pores and UH particles.

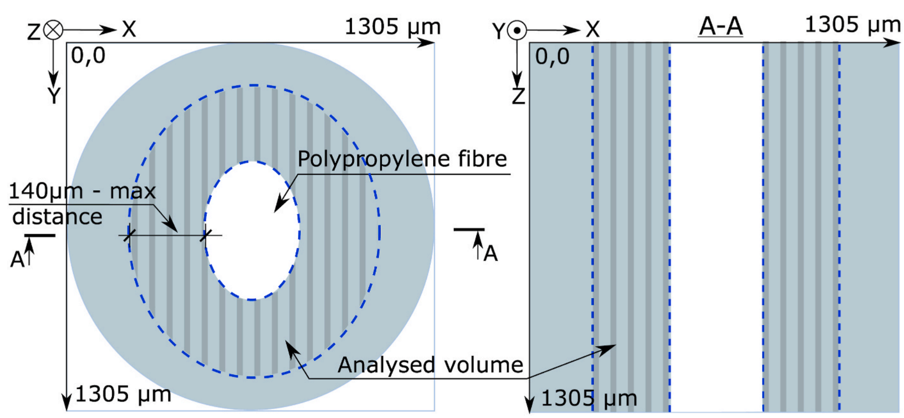

Fig. 10. The location of the fibre in the sample. Blue dashed lines indicate the volume of the cement-paste that was analysed to define the distributions of pores and UH particles. (For interpretation of the references to colour in this figure legend, the reader is referred to the Web version of this article.)

Table 2
The volume fractions of pores measured in the whole sample volumes.

Sample	Vol. of pores, mm^3	Vol. of cement-paste, mm^3	Vol. frac. of pores, %
S1	0.08	1.35	5.93
S2	0.04	1.35	2.96
S3	0.10	1.35	7.41

Table 3
The volume fractions of pores measured within the distance from 0 to 140 μm from the fibre surface.

Sample	Vol. of pores, mm^3	Vol. frac. of pores, %	Vol. of pores, mm^3	Vol. frac of pores, %	Vol. frac. of pores, %
	0 – 70 μm	0 – 70 μm	70 – 140 μm	70 – 140 μm	0 – 140 μm
S1	0.018	8.3	0.015	5.45	6.8
S2	0.010	4.6	0.006	2.34	3.4
S3	0.041	20.1	0.014	4.76	11.8

In the thresholding method for image segmentation, the particles between the minimum and maximum values of the gray-level thresholds are selected and all the other gray-level values are disregarded. In Ref. [28,44,45], this method was used to identify hydrated and UH particles and pores from the cement paste. Possible approaches for selecting the gray-level thresholds to separate material components are: manual thresholding, tangent-slope and overflow criterion including the cumulative curve of the gray-level image. Manual thresholding is based on subjective visual perception of threshold boundaries and depends on the operator [33]. The tangent-slope approach can be utilised, when the local minima in the gray-level histogram are implicit. In the study reported in Ref. [36], the tangent-slope approach was used to separate the pores and the hydration products (HP) of the OP cement paste based on the gray-level histogram, where the distribution of pixels representing the pores had no distinct peak. In the researches [44,45], the gray-level threshold separating the HP from UH particles was defined as a point, where a change of tangent-slope to a decreasing side of the gray-level histogram occurred. The global peak of the histogram

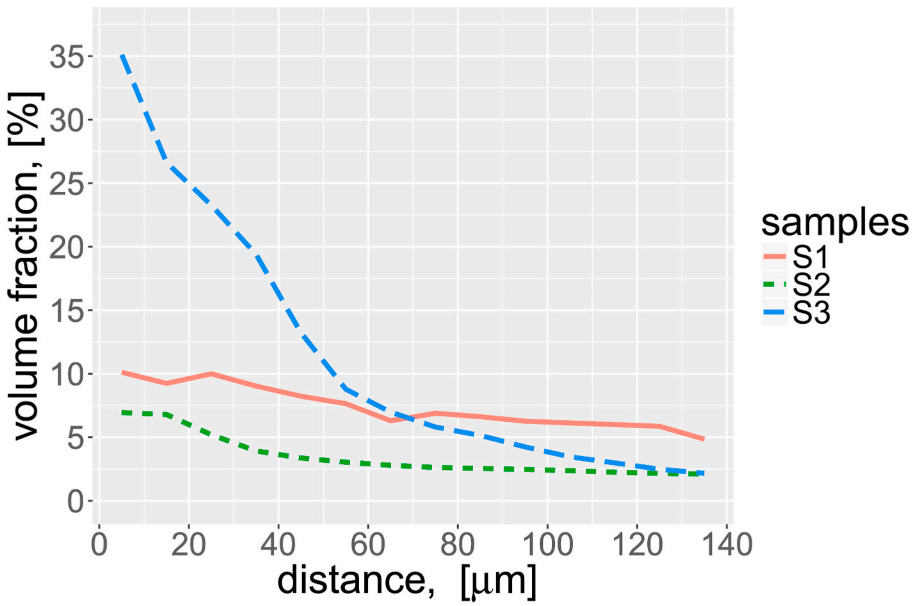

Fig. 11. The distributions of the volume fractions of pores within the distance from 0 to 140 μm from the fibre surface.

corresponded to HP and was followed by a sudden decrease in the distribution. A slight increase of the distribution function after the global peak was due to the increased number of pixels representing the UH particles, and was indicating the change of tangent. The similar behaviour of the gray-level histogram can be observed in Fig. 6. The study referred in Ref. [42] introduced an overflow criterion approach to separate the pores and HP, and also used the cumulative curve of the gray-level image. The value of the gray-level threshold at which the area of pixels representing the pores started to overflow to the surrounding areas was defined as a critical value providing a good estimate for the pore threshold level. This boundary also coincided with the intersection point of tangents to the first inflection point of cumulative curve. However, the overflow criterion may slightly overestimate the true overflow point.

In present study, the overflow criterion with the combination of tangent-slope approach were used to determine the gray-level thresholds of pores and UH particles. CT images were processed by ImageJ, which is an image processing program designed for scientific multidimensional images [1], and the image processing package Fiji based on ImageJ [34,35].

The pores were the darkest regions in CT images. The lower threshold of pores was defined as equal to 0, since pores can be totally empty of any material. Fig. 4 represents the thresholds of pores considering the overflow criterion according to which the upper threshold in all the samples was varying between the gray-level values of 60 and 70, which indicated that the pores could contain some water. The brightest particles in CT images of the cement paste should be the UH clinker, slag and limestone powder grains due to their higher densities compared to HP. The clinker grains, such as alite, belite, alumoferrit have mass densities over 3100 kg/m^3, while the mass densities of slag and limestone powder are 2900 kg/m^3 and 2700 kg/m^3, respectively [4,11,38]. The mass density of typical hydration products, such as CSH gel, CAH, ettringite, monosulphate-type phases, calcium carbo-aluminate hydrates, calcium hydroxide, etc. are ranging between 1440 and 2240 kg/m^3 [38,39], which is distinctly less than the mass densities of the unhydrated cement grains. The upper threshold of UH particles was defined as a maximum value of the gray-level and was equal to 255. The lower thresholds of UH particles were adjusted with the overflow criterion, which gave the gray-level ranges of 160–170, 140–150 and 160–170 for the samples S1, S2 and S3, respectively, as illustrated in Fig. 5.

The cumulative curves of the gray-level images represented in Fig. 6 (a), (b), (c), Fig. 6, demonstrate the intersection points of the tangents to the first inflection points of the cumulative curves, which correspond to the thresholds separating the pores and HP. The intersection points gave for the upper thresholds of pores the values of 69, 70 and 71 in the samples S1, S2 and S3, respectively. Using the tangent-slope approach, the lower threshold of UH particles was defined as the intersection point of tangents between the decreasing curve of the gray-level histogram and the slight increment of the distribution. In Fig. 6(a), (b), (c) these intersection points were at 153, 142, 158 in the samples S1, S2 and S3, respectively, and they presented the lower thresholds of UH particles.

To support the initial thresholds selected using the overflow criterion, cumulative curve, and tangent-slope approach, the threshold levels of pores and UH particles were also measured based on the gray-level histograms along the lines crossing the individual particles (Fig. 7). Measuring the thresholds along the lines gave the upper values of 49, 53 and 55 for pores and the lower values of 161, 154 and 163 for UH particles in the samples S1, S2 and S3, respectively.

The final selection of the thresholds for pores and UH particles to segment the volume images was calculated as averages of all the threshold values defined by different approaches. For example, the threshold for pores in the sample S1 was 60 or 70 based on Fig. 4 and 69 based on Fig. 6 and 49 based on Fig. 7, and the average of these four numbers gave 62 for the final threshold for pores in the sample S1. The final upper thresholds of pores in the samples S2 and S3 were 63, 64, respectively. The final lower thresholds of UH particles were 161, 147, 163 in the samples S1, S2 and S3, respectively. Examples of slices with pores and UH particles identified based on these gray-levels are represented in Fig. 8.

The pores and UH particles were segmented and binarised with the "Threshold" tool using the final gray-levels represented in Fig. 8. The fibre was isolated from the two-dimensional slices, so that only the cement paste remained in the image. A three-dimensional visualisation of the segmented pores and UH particles in the sample S3 is represented in Fig. 9.

3. Results and discussion

3.1. Results

The quantification of segmented particles for statistical analysis was

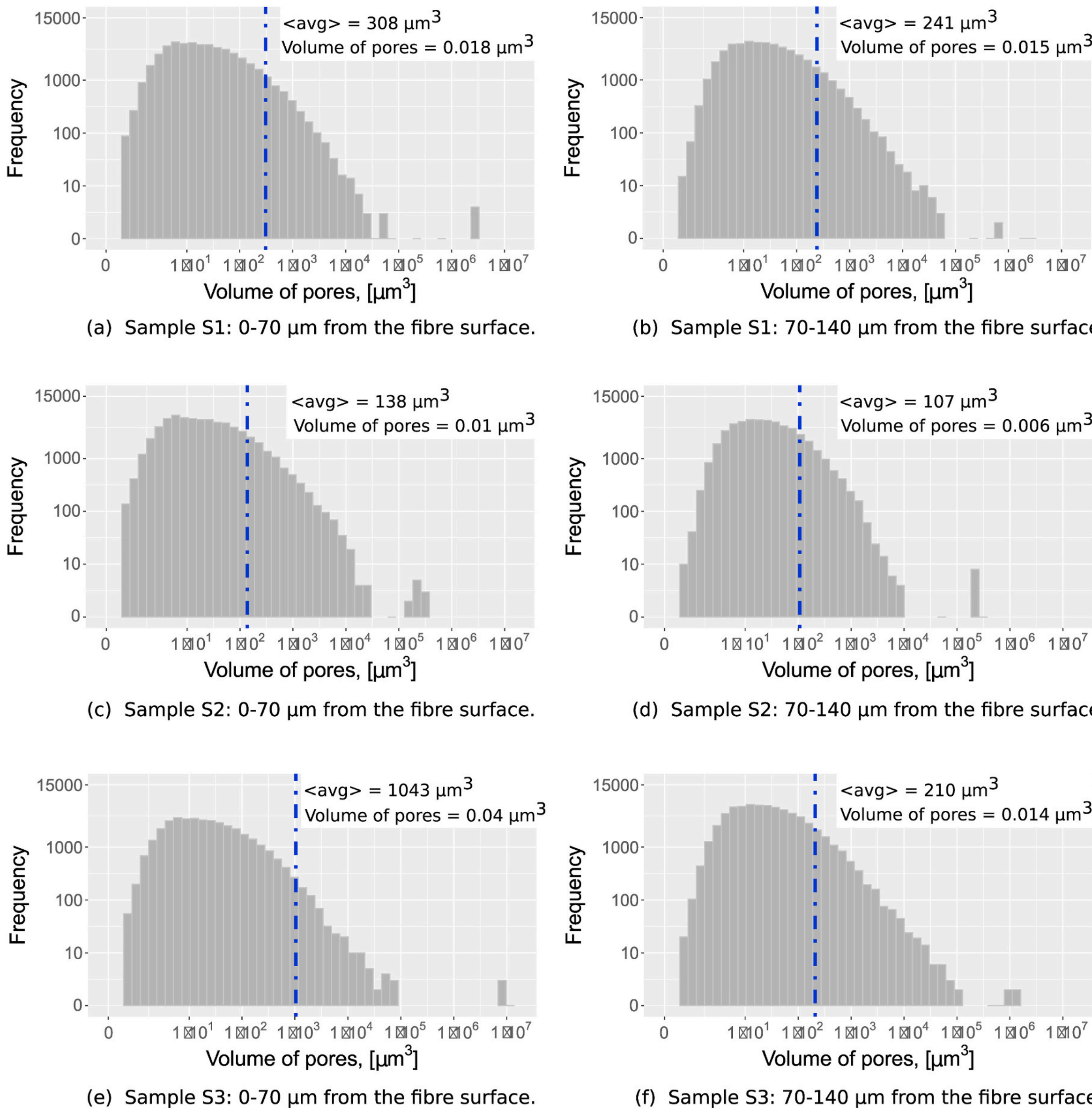

(a) Sample S1: 0-70 µm from the fibre surface.
(b) Sample S1: 70-140 µm from the fibre surface.
(c) Sample S2: 0-70 µm from the fibre surface.
(d) Sample S2: 70-140 µm from the fibre surface.
(e) Sample S3: 0-70 µm from the fibre surface.
(f) Sample S3: 70-140 µm from the fibre surface.

Fig. 12. The distributions of pore volumes from the fibre surface.

Table 4
The volume fractions of UH particles identified in the whole sample volumes.

Sample	Vol. of UH, mm^3	Vol. of cement-paste, mm^3	Vol. frac. of UH, %
S1	0.069	1.35	5.13
S2	0.065	1.35	4.77
S3	0.063	1.35	4.64

Table 5
The volume fractions of UH particles identified within the range up to 140 μm from the fibre surface.

Sample	Vol. frac. of UH, %	Vol. frac of UH, %	Vol. frac. of UH, %
	0 – 70 μm	70 – 140 μm	0 – 140 μm
S1	4.8	6.0	5.5
S2	4.8	5.6	5.3
S3	4.0	5.6	4.9

made by “3D Roi Manager” plugin [26] in the 3D ImageJ Suite developed for ImageJ/Fiji. The plugin was applied on the three-dimensional stacks, which were made of two-dimensional slices (Fig. 9). “3D Roi Manager” plugin can calculate the geometrical characteristics, such as the volume and surface area of the segmented three-dimensional objects with arbitrary shape, which is important feature, since pores and UH particles generally have irregular forms. The percentages of the volume fractions of pores and UH particles were calculated by “Voxel counter” plugin [31]. The analysis of quantitative data was made by R-programming language [29]. The location of the fibre in the sample and the outer boundary of the area around the fibre used to compile distributions for pores and UH particles are given in Fig. 10.

The average volume fractions of pores calculated from the whole samples are given in Table 2. The volume fractions of pores and their distributions from 0 to 140 μm from the fibre surface are represented in Table 3 and Fig. 11. In all the three samples, a considerable change in the distributions appeared approximately at a distance of 70 μm from the fibre surface, which indicated the range of the boundary zone created by the fibre. The main feature was that the pore content increased towards the fibre surface. The porosity of the whole sample and the porosity of

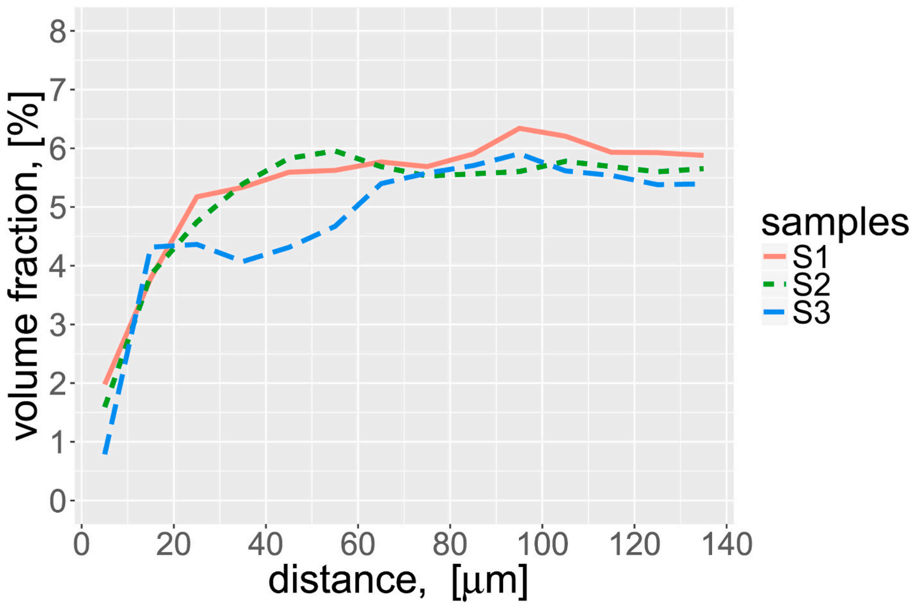

Fig. 13. Distribution of the volume fraction of UH particles within the range up to 140 μm from the fibre surface.

the bulk cement paste, i.e. from 70 – 140 μm from the fibre surface, matched well with the samples S1 and S2, as observed in Tables 2 and 3. In the sample S3 within the boundary zone, i.e. from 0– 70 μm from the fibre surface, the porosity was considerably increased, which explains the difference of porosity of the bulk cement paste in Table 2 from the porosity in Table 3. The distributions of pore volumes within the distances from 0 to 70 μm and from 70 to 140 μm from the fibre surface are represented in Fig. 12 and can be assessed together with Fig. 8. Based on Fig. 12 (a), (c), (e), the fraction of pores with the volume of more than 10^5 μm^3 was greater in the boundary zone than in the bulk cement paste. The mean values of the pore volumes within the interval from 0 to 70 μm from the fibre surface were 308 μm^3, 138 μm^3 and 1043 μm^3 in the samples S1, S2 and S3, respectively. In the bulk cement paste, i.e. within the interval from 70 to 140 μm from the fibre surface, the mean values of the pore volumes were 241 μm^3, 107 μm^3 and 210 μm^3 in the samples S1, S2 and S3, respectively.

The average volume fractions of UH particles identified in the whole samples are given in Table 4. The volume fractions of UH particles and their distributions with a range from 0 to 140 μm from the fibre surface are represented in Table 5 and Fig. 13, respectively. These results also confirmed that the width of boundary zone was about 60– 70 μm from the fibre surface. In all the samples, the fractions of UH practices were quite similar with a decreasing tendency towards the fibre surface. In the whole sample the fraction of UH particles (Table 4) was slightly lower compared to the bulk cement paste, i.e. the range between 70 and 140 μm in Table 5.

3.2. Discussion

In the hardened cement paste, the fibre-created boundary zone was recognised from the distributions of the volume fractions of pores and UH particles. The volume fractions of pores were defined based on the occurrence of volumes without any or with low mass density, while the UH particles represented the volumes of high mass density. At a distance of about 60 – 70 μm from the fibre surface, a clear decrease in the gradients of the distributions compiled for the volumes of both, the pores and UH particles, were observed. This change was a marker of the boundary between the ITZ and the bulk cement paste.

The geometry of pores appeared to be complicated and interconnected. The definition of an isolated pore is subjected to the spatial resolution achieved by CT equipment. An interconnected structure of capillary pores was also mentioned in Ref. [6], where the authors noted that an increased content of capillary pores and their interconnection lead to increased permeability in the boundary zone. The higher porosity close to the fibre surface, especially in sample S3, can be a consequence of hydrophobic properties of polypropylene fibre. In cementitious mixtures with polypropylene fibres the tendency of formation of large air voids with uneven distribution was reported in Ref. [16]. In the present work in the range up to 70 μm from the fibre surface, the relative amount of pores of larger volumes was greater than in the bulk cement paste.

The results obtained by SEM method in Ref. [21] indicated that the width of the ITZ around the aggregate in concrete is about 60 – 70 μm. In the cement paste around the steel fibres with diameters of 0.2 and 0.4 mm, the width of the transition zone varied between 40 and 70 μm in the study reported in Ref. [37]. In Ref. [43] the width received for the transition zone varied between 25 and 30 μm around the steel fibres and was 15 μm around the polypropylene fibres, when the diameters of the steel and polypropylene fibres were 0.5 mm and 30 μm, respectively. The width of the boundary zone defined in this study lies close to the upper limit of the range observed in earlier studies, which may partly be explained by the accuracy of the phase contrast tomography. However, it is also obvious that this particular mixture of cement, slag, and limestone does not reduce the width of the boundary zone.

The surface characteristics of fibre can affect the formation of the boundary zone. For example, the roughness profile along the perimeter of steel fibres measured in Ref. [7] revealed that the particles touching the fibre can create empty spaces, which may be filled with particles of fine or ultra fine cementitious materials. This can lead to a decreased width of the ITZ, which was reported in Refs. [22]. If empty spaces are filled with particles, a smaller amount of water accumulates close to the inclusion surface, which may lead to reduced porosity and denser micro-structure. The type of fibre material can also influence the ITZ. In Ref. [43] the authors confirmed that due to the hydrophobicity of polypropylene fibres the concentration of pores close to the fibre surface was increased. The results presented in Ref. [30] also highlighted the hydrophobic properties of polypropylene fibres, which promoted the repelling of water and resulted in weak contact between the fibres and geopolymer matrix. In Ref. [20] it was concluded that the electric properties of the inclusion can affect the interaction with fresh cement paste, which usually contains charged particles.

4. Conclusions

This study confirmed that the phase contrast tomography is a suitable method to study the boundary zone around the fibre in the hardened cement paste. The main findings of the study are:

- in the hardened cement paste the boundary zone around the polypropylene fibre extended to a distance of 70 μm from the fibre surface;
- the mixture of cement, slag, and limestone has not observed to decrease the width of the boundary zone around the polypropylene fibre;
- the volume fraction of pores was increasing towards the polypropylene fibre surface. In two samples the relative amount of pores close to the fibre was almost doubled and in one sample it was four times more compared to the bulk cement paste;
- the amount of pores with the volume exceeding 10^5 μm^3 increased within the ITZ compared to bulk cement paste;
- the volume of UH particles decreased about 67% towards the polypropylene fibre surface in all the samples.

Declaration of competing interest

The authors declare that they have no known competing financial interests or personal relationships that could have appeared to influence the work reported in this paper.

Acknowledgement

The research was supported by Auramo-Säätiö foundation. The research leading to these results received funding from the “Academy of Finland Post-doctoral Researcher” grant number 289740. The support from Doctoral Program of the School of Engineering of Aalto University is gratefully acknowledged.

References

[1] M.D. Abramoff, P.J. Magalhaes, S.J. Ram, Image processing with ImageJ, BI 11 (2004) 36–42.
[2] P. Barnes, J. Bensted, Structure and Performance of Cements, second ed., Taylor & Francis, 2002. https://books.google.fi/books?id=6wPpkyrWE5oC.
[3] A. Bentur, S. Mindess, Fibre Reinforced Cementitious Composites, second ed., Taylor & Francis, 2007.
[4] D. Bentz, A. Ardani, T. Barrett, S. Jones, D. Lootens, M. Peltz, T. Sato, P. Stutzman, J. Tanesi, W. Weiss, Multi-scale investigation of the performance of limestone in concrete, Construct. Build. Mater. 75 (2014), https://doi.org/10.1016/j.conbuildmat.2014.10.042.
[5] D.P. Bentz, S. Mizell, S. Satterfield, J. Devaney, W. George, P. Ketcham, J. Graham, J. Porterfield, D. Quenard, F. Vallee, H. Sallee, E. Boller, H. Baruchel, The visible cement data set, J. Res. Natl. Inst. Stan. 107 (2002) 137–148, https://doi.org/10.6028/jres.107.013.
[6] S. Diamond, J. Huang, The interfacial transition zone: reality or myth?, in: RILEM Proceedings CRC Press, London, 1998, pp. 3–42, https://doi.org/10.1201/9781482295085.
[7] M. Eik, A. Antonova, J. Puttonen, Roughness of steel fibre and composition of cement paste close to fibre surface, J. Adv. Concr. Technol. 17 (2019) 628–638, https://doi.org/10.3151/jact.17.628.
[8] D. Fall, K. Lundgren, R. Rempling, K. Gylltoft, Reinforcing tailor-made concrete structures: alternatives and challenges, Eng. Struct. 44 (2012) 372–378, https://doi.org/10.1016/j.engstruct.2012.06.003.
[9] O.Y. Finnsementti, Kj400 ground granulated blastfurnace slag: technical data sheet. http://www.finnsementti.fi, 2016.
[10] O.Y. Finnsementti, Plussementti: technical data sheet. http://www.finnsementti.fi, 2016.
[11] O.Y. Finnsementti, Plussementti: masuunikuonajauhe kj400. http://www.finnsementti.fi, 2019.
[12] E. Gallucci, K. Scrivener, A. Groso, M. Stampanoni, G. Margaritondo, 3d experimental investigation of the microstructure of cement pastes using synchrotron x-ray microtomography, Cement Concr. Res. 37 (2007) 360–368, https://doi.org/10.1016/j.cemconres.2006.10.012.
[13] G.L. Guerrini, Applications of high-performance fiber-reinforced cement-based composites, Appl. Compos. Mater. 7 (2000) 195–207, https://doi.org/10.1023/A:1008994020916.
[14] T. Henriksen, S. Lo, U. Knaack, An innovative approach to manufacture thin-walled glass fibre reinforced concrete for tomorrow's architectural buildings envelopes with complex geometries, J. Build. Eng. 4 (2015) 189–199, https://doi.org/10.1016/j.jobe.2015.09.006.
[15] D. Hernàndez-Cruz, C.W. Hargis, S. Bae, P.A. Itty, C. Meral, J. Dominowski, M. J. Radler, D.A. Kilcoyne, P.J. Monteiro, Multiscale characterization of chemical-mechanical interactions between polymer fibers and cementitious matrix, Cement Concr. Compos. 48 (2014) 9–18, https://doi.org/10.1016/j.cemconcomp.2014.01.001.
[16] D. Hernàndez-Cruz, C.W. Hargis, J. Dominowski, M.J. Radler, P.J. Monteiro, Fiber reinforced mortar affected by alkali-silica reaction: a study by synchrotron microtomography, Cement Concr. Compos. 68 (2016) 123–130, https://doi.org/10.1016/j.cemconcomp.2016.02.003.
[17] H. Justnes, Influence of scms on hydration and durability of blended cements: chemical and physical principles, J. Chin. Ceram. Soc. 43 (2015) 1359, https://doi.org/10.14062/j.issn.0454-5648.2015.10.06.
[18] P. Kalifa, G. Chene, C. Galle, High-temperature behaviour of hpc with polypropylene fibres: from spalling to microstructure, Cement Concr. Res. 31 (2001) 1487–1499, https://doi.org/10.1016/S0008-8846(01)00596-8.
[19] E.N. Landis, D.T. Keane, X-ray microtomography, Mater. Char. 61 (2010) 1305–1316, https://doi.org/10.1016/j.matchar.2010.09.012.
[20] A. Lavrov, E.A.C. Panduro, M. Torsater, Synchrotron study of cement hydration: towards computed tomography analysis of interfacial transition zone, Energy Procedia 114 (2017) 5109–5117, https://doi.org/10.1016/j.egypro.2017.03.1666. 13th International Conference on Greenhouse Gas Control Technologies. GHGT-13, 14-18 November 2016, Lausanne, Switzerland.
[21] A. Leemann, B. Munch, P. Gasser, L. Holzer, Influence of compaction on the interfacial transition zone and the permeability of concrete, Cement Concr. Res. 36 (2006) 1425–1433, https://doi.org/10.1016/j.cemconres.2006.02.010.
[22] P.K. Mehta, P.J.M. Monteiro, Effect of aggregate, cement, and mineral admixtures on the microstructure of the transition zone, MRS Proc. 114 (1987) 65, https://doi.org/10.1557/PROC-114-65.
[23] A. Momose, T. Takeda, A. Yoneyama, I. Koyama, Y. Itai, Phase-contrast x-ray imaging using an x-ray interferometer for biological imaging, Anal. Sci. (Supplements 17icas) (2002), https://doi.org/10.14891/analscisp.17icas.0.i527.0 i527–i530.
[24] A. Noumowe, Mechanical properties and microstructure of high strength concrete containing polypropylene fibres exposed to temperatures up to 200 deg, Cement Concr. Res. 35 (2005) 2192–2198, https://doi.org/10.1016/j.cemconres.2005.03.007.
[25] Novitom, Novitom brochure. http://www.novitom.com, 2015.
[26] J. Ollion, J. Cochennec, F. Loll, C. Escude, T. Boudier, Tango: a generic tool for high-throughput 3d image analysis for studying nuclear organization, Bioinformatics 29 (2013) 1840–1841, https://doi.org/10.1093/bioinformatics/btt276.
[27] D. Paganin, S.C. Mayo, T.E. Gureyev, P.R. Miller, S.W. Wilkins, Simultaneous phase and amplitude extraction from a single defocused image of a homogeneous object, J. Microsc. 206 (2002) 33–40, https://doi.org/10.1046/j.1365-2818.2002.01010.x.
[28] M.A.B. Promentilla, T. Sugiyama, T. Hitomi, N. Takeda, Characterizing the 3d pore structure of hardened cement paste with synchrotron microtomography, J. Adv. Concr. Technol. 6 (2008) 273–286, https://doi.org/10.3151/jact.6.273.
[29] R Development Core Team, R: A Language and Environment for Statistical Computing, R Foundation for Statistical Computing, Vienna, Austria, 2011. URL, http://www.R-project.org.
[30] N. Ranjbar, S. Talebian, M. Mehrali, C. Kuenzel, H.S.C. Metselaar, M.Z. Jumaat, Mechanisms of interfacial bond in steel and polypropylene fiber reinforced geopolymer composites, Compos. Sci. Technol. 122 (2016) 73–81, https://doi.org/10.1016/j.compscitech.2015.11.009.
[31] W. Rasband, ImageJ URL. https://imagej.nih.gov/ij/, 1997-2016.
[32] U. Rattanasak, K. Kendall, Pore structure of cement/pozzolan composites by x-ray microtomography, Cement Concr. Res. 35 (2005) 637–640, https://doi.org/10.1016/j.cemconres.2004.04.022.
[33] J.C. Russ, in: The Image Processing Handbook, Fifth Edition (Image Processing Handbook), CRC Press, Inc., Boca Raton, FL, USA, 2006.
[34] J. Schindelin, I. Arganda-Carreras, E. Frise, V. Kaynig, M. Longair, T. Pietzsch, S. Preibisch, C. Rueden, S. Saalfeld, B. Schmid, J.Y. Tinevez, D.J. White, V. Hartenstein, K. Eliceiri, P. Tomancak, A. Cardona, Fiji: an open-source platform for biological-image analysis, Nat. Methods 9 (2012) 676–682. URL, http://search.ebscohost.com/login.aspx?direct=true&db=asn&AN=77406531&site=ehost-live&authtype=sso&custid=ns192260.
[35] J. Schindelin, C.T. Rueden, M.C. Hiner, K.W. Eliceiri, The imagej ecosystem: an open platform for biomedical image analysis, Mol. Reprod. Dev. 82 (2015) 518–529, https://doi.org/10.1002/mrd.22489.
[36] K.L. Scrivener, H.H. Patel, P.L. Pratt, L.J. Parrott, Analysis of phases in cement paste using backscattered electron images, methanol adsorption and thermogravimetric analysis, MRS Proc. 85 (1986) 67, https://doi.org/10.1557/PROC-85-67.
[37] Y. Shao, Z. Li, S.P. Shah, Matrix cracking and interface debonding in fiber-reinforced cement-matrix composites, Adv. Cement Base Mater. 1 (1993) 55–66, https://doi.org/10.1016/1065-7355(93)90010-L.
[38] H. Taylor, Cement Chemistry, Thomas Telford, 1997. URL, https://books.google.fi/books?id=1BOETtwi7mMC.
[39] P.D. Tennis, H.M. Jennings, A model for two types of calcium silicate hydrate in the microstructure of portland cement pastes, Cement Concr. Res. 30 (2000) 855–863, https://doi.org/10.1016/S0008-8846(00)00257-X.

[40] Y.S. Wang, J.G. Dai, X-ray computed tomography for pore-related characterization and simulation of cement mortar matrix, NDT E Int. 86 (2017) 28–35, https://doi.org/10.1016/j.ndteint.2016.11.005.
[41] M.J. Willemink, P.B. Noël, The evolution of image reconstruction for ct—from filtered back projection to artificial intelligence, Eur. Radiol. 29 (2019) 2185–2195, https://doi.org/10.1007/s00330-018-5810-7.
[42] H. Wong, M. Head, N. Buenfeld, Pore segmentation of cement-based materials from backscattered electron images, Cement Concr. Res. 36 (2006) 1083–1090, https://doi.org/10.1016/j.cemconres.2005.10.006.
[43] L. Xu, F. Deng, Y. Chi, Nano-mechanical behavior of the interfacial transition zone between steel-polypropylene fiber and cement paste, Construct. Build. Mater. 145 (2017) 619–638, https://doi.org/10.1016/j.conbuildmat.2017.04.035.
[44] H. Zhang, B. Šavija, S. Chaves Figueiredo, M. Lukovic, E. Schlangen, Microscale testing and modelling of cement paste as basis for multi-scale modelling, Materials 9 (2016) 907, https://doi.org/10.3390/ma9110907.
[45] M. Zhang, Y. He, G. Ye, D.A. Lange, K. van Breugel, Computational investigation on mass diffusivity in portland cement paste based on x-ray computed microtomography (mct) image, Construct. Build. Mater. 27 (2012) 472–481, https://doi.org/10.1016/j.conbuildmat.2011.07.017.